

A scalable multi-photon coincidence detector based on superconducting nanowires

Di Zhu¹, Qing-Yuan Zhao^{1,2*}, Hyeonrak Choi¹, Tsung-Ju Lu¹, Andrew E. Dane¹, Dirk Englund¹ and Karl K. Berggren^{1*}

Coincidence detection of single photons is crucial in numerous quantum technologies and usually requires multiple time-resolved single-photon detectors. However, the electronic readout becomes a major challenge when the measurement basis scales to large numbers of spatial modes. Here, we address this problem by introducing a two-terminal coincidence detector that enables scalable readout of an array of detector segments based on superconducting nanowire microstrip transmission line. Exploiting timing logic, we demonstrate a sixteen-element detector that resolves all 136 possible single-photon and two-photon coincidence events. We further explore the pulse shapes of the detector output and resolve up to four-photon events in a four-element device, giving the detector photon-number-resolving capability. This new detector architecture and operating scheme will be particularly useful for multi-photon coincidence detection in large-scale photonic integrated circuits.

Single-photon detection plays a key role in quantum information processing, including modular quantum computing with trapped ions¹ and solid-state quantum emitters^{2–4}, photonic quantum walks and Boson sampling^{5–8}, quantum simulations⁹ and linear optical quantum computing¹⁰. Most of these applications rely on coincidence measurement of single or entangled photons over a large number of spatial modes and require an equal number of time-resolved single-photon detectors. Among various single-photon detectors¹¹, the superconducting nanowire single-photon detector (SNSPD) has become increasingly attractive because of its outstanding detector metrics^{12–16} and feasibility of on-chip integration^{17–23}. Traditional SNSPD arrays used for space communication²⁴, photon number resolution²⁵ and few-channel coincidence counting²¹ adopt parallel readout of individual detector elements. However, scaling these arrays for coincidence counting over large numbers of channels presents formidable challenges, especially for the electrical readout²⁶.

A number of multiplexing schemes and device architectures have been developed to solve the readout problem. Row–column multiplexing is an efficient scheme but still requires $2N$ readout channels for N^2 pixels²⁷. Another promising scheme is the frequency-division multiplexing, where SNSPDs are embedded in resonators operating at different radio-frequency (RF) tones^{28,29}. Though a common feed line can couple multiple resonators, each RF tone needs a demultiplexing circuit. Besides frequency-domain multiplexing, time-domain multiplexing has also been explored. Time-tagged multiplexing has been demonstrated in a proof-of-concept two-element array³⁰, in which the signals from the two elements were separated in time using a delay line. Though this approach only required a single readout line, the device dimension and array size were limited by the delay line design. Time-tagged multiplexing was more recently employed to create a single-photon imager from a continuous nanowire delay line³¹. This imager resolves photon position but is only used to detect one photon at a time. Another architecture connects nanowires in parallel and encodes the desired information in the amplitude of the electrical output, such as photon number³² or position³³. However, these detectors require on-chip resistors for

biasing, and the array size is limited by the leakage current to the parallel branches.

Here, we report on a two-terminal detector based on superconducting nanowire microstrip transmission lines that works as a scalable array. Unlike previous work^{30,31}, this detector resolves the location of more than one photon and works naturally as a coincidence counter. With simple timing logic, we demonstrated the resolution of all 136 possible single- and two-photon events in a sixteen-element detector. With pulse shape processing, we resolved up to fourfold coincidence events and showed photon-number-resolving capability in a four-element device. The microstrip transmission line used in the detector had a group velocity as low as $0.016c$ (where c is the speed of light in vacuum) and may allow denser packing compared to co-planar structures³¹. The detector was designed for integration on optical waveguide arrays and fabricated on a waveguide-compatible substrate material. We expect it to find immediate applications in large-scale on-chip coincidence detection for quantum information processing.

Device architecture

Figure 1 illustrates the basic architecture and operating principle of the detector. In our design, individual detecting elements were connected by nanowire delay lines, resulting in a one-dimensional detector array. Figure 1a shows the physical implementation of a sixteen-element (D_1 to D_{16}) array. The fabrication is described in the Methods section. The detectors and delay lines were patterned from a ~ 5 -nm-thick niobium nitride (NbN) film on aluminum nitride (AlN)-on-sapphire substrate³⁴. Figure 1a(i) shows a scanning electron micrograph (SEM) of the delay line. Each meandered delay line had a width of 300 nm, a period of $1.8\ \mu\text{m}$ and a total length of $429\ \mu\text{m}$. Figure 1a(ii) shows an SEM of a detector segment. Each detector segment consisted of a pair of 80-nm-wide, $5\text{-}\mu\text{m}$ -long parallel nanowires. This detector segment design is known as a two-element superconducting nanowire avalanche photodetector (2-SNAP)³⁵. Compared to a standard hairpin nanowire¹⁸, the 2-SNAP enhanced signal-to-noise ratio and provided relatively good impedance matching to the 300-nm-wide delay lines. To make the nanowires

¹Research Laboratory of Electronics, Massachusetts Institute of Technology, Cambridge, MA, USA. ²Research Institute of Superconductor Electronics, School of Electronic Science and Engineering, Nanjing University, Nanjing, Jiangsu, China. *e-mail: qyzhao@nju.edu.cn; berggren@mit.edu

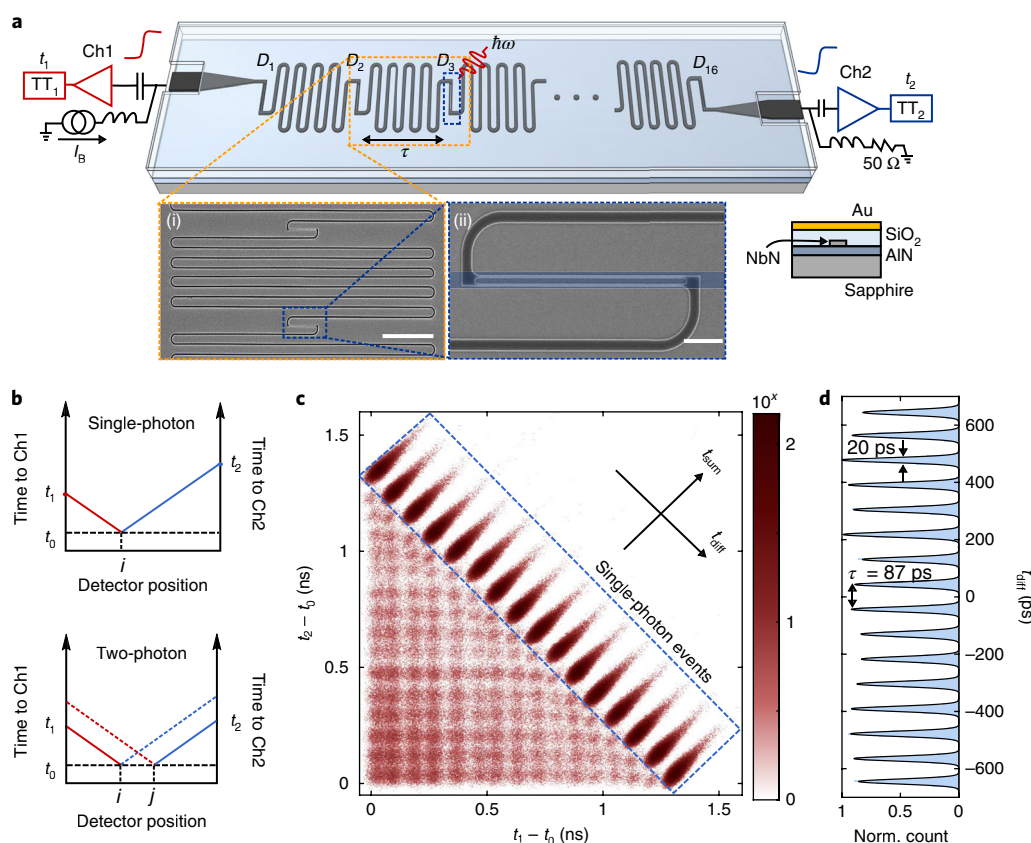


Fig. 1 | Device architecture and operating mechanism. **a**, Device layout for a sixteen-element detector. The detector is a two-terminal array that connects a chain of single-photon detector segments using slow-wave nanowire delay lines. The nanowire was designed to be a microstrip waveguide with a dielectric spacer and a top ground plane. (i) SEM of the delay line, which consisted of a 300-nm-wide meandered nanowire. Scale bar, 10 μm . (ii) SEM of a detector segment, which consisted of two 80-nm-wide parallel nanowires. Scale bar, 1 μm . The blue band marks the site for future waveguide integration. TT, time tagger. **b**, Illustration of the timing logic in the detector. *t*₀ is the photon arrival time; *t*₁ and *t*₂ are the times when the electrical signal arrives at Ch1 and Ch2, respectively. **c**, Measured timing distribution that resolved all 136 distinguishable groups. The histogram was constructed from one million detection events. The colour bar represents number of events per time bin (log scale) with a bin size of ~ 3 ps. **d**, A 1D histogram of the difference time (*t*_{diff} = (*t*₁ - *t*₂)/2) when the detector was operating in the single-photon regime. The standard deviation of the peak amplitudes was 6% of their mean, indicating a uniform efficiency of the segments. The average FWHM differential jitter was 20 ps and timing delay between adjacent segments was 87 ps. Data in **c,d** were measured using a sub-ps pulsed laser at 1,550 nm.

into transmission lines, we capped the device area with a 450-nm-thick oxide spacer and 60-nm-thick gold ground plane on the top (see Supplementary Fig. 2 for micrographs of the overall device). Designing the isolated nanowires as transmission lines was essential for the delay-line-based detector: the transmission line guided the RF signal along the nanowire with a slow propagation speed and minimized RF coupling in the meander. The current device design was designed for future integration with a sixteen-channel AlN photonic waveguide array (see Supplementary Section 4). The blue shaded band in Fig. 1a(ii) marks the potential position for an optical waveguide.

The detector was biased using a constant current and read out on both terminals (Ch1 and Ch2) using room-temperature low-noise amplifiers^{31,36}. When the 2-SNAP was biased close to its critical current, the delay line was only biased at $\sim 50\%$ and therefore would not respond to incident photons.

Figure 1b illustrates the timing logic in the detector. In the single-photon regime (see the upper panel in Fig. 1b), only one segment fires at a time, following the timing logic as presented in refs.^{30,31}. For instance, if a photon arrives on the *i*th detector *D_i* at time *t*₀ and excites a pair of counter-propagating pulses, the left-propagating pulse will reach Ch1 at time *t*₁ = *t*₀ + (*i* - 1) τ , where τ

is the delay between two adjacent segments; and the right-propagating pulse will reach Ch2 at time *t*₂ = *t*₀ + (*N* - *i*) τ , where *N* is the number of segments in the array. In this case, the arrival time of the photon can be derived from the sum of the two pulse times, (*t*₁ + *t*₂)/2 = *t*₀ + (*N* - 1) τ /2, while the arrival location of the photon is determined from their difference, (*t*₁ - *t*₂)/2 τ = *i* - (*N* + 1)/2.

The timing logic is different for the two-photon case (see the lower panel in Fig. 1b). When two segments fire at the same time, each of them launches a pulse pair, but each readout channel will only identify the pulse edge from its nearest segment because the pulse width (ns) is significantly larger than the delay time (ps). So if *D_i* and *D_j* both fire (*i* < *j*), Ch1 will tag *t*₁ = *t*₀ + (*i* - 1) τ , while Ch2 will tag *t*₂ = *t*₀ + (*N* - *j*) τ . If *t*₀ is known, one can trace back both *i* and *j*. This method requires the knowledge of *t*₀, which is available in many practical applications. For pulsed single-photon or photon-pair sources, the excitation laser gives *t*₀; in communication or computing, the reference clock gives *t*₀ as long as the timing window and timing jitter are smaller than τ .

Demonstration of a sixteen-element detector

Figure 1c shows the measured timing distribution in a sixteen-element detector. 136 groups of detection events can be distinguished.

The diagonal groups correspond to the 16 single-photon detection cases, and the off-diagonal groups correspond to the 120 (C_2^{16}) two-photon detection cases. Like all array-type photon-number-resolving detectors, the cases where two photons hit the same detector (with probability $O(1/N)$) cannot be resolved. The observed higher counting rate at $t_1 - t_0$ and $t_2 - t_0$ near zero (lower-left corner in the histogram) was because these detection groups included more three-or-more photon events. More details on beyond two-photon detection will be discussed later. The histogram was constructed from one million detection events, discretized here in bins of ~ 3 ps. The detector was measured at 3.0 K and flood-illuminated from the back of the chip using a 1,550 nm sub-ps pulsed laser. It was biased at 14.5 μ A with a switching current of 15.3 μ A.

It is useful to introduce two characteristic timing variables: the sum time, $t_{\text{sum}} = (t_1 + t_2)/2 - t_0$, and the difference time, $t_{\text{diff}} = (t_1 - t_2)/2$. ($t_{\text{sum}}, t_{\text{diff}}$) forms a basis that is rotated relative to the ($t_1 - t_0, t_2 - t_0$) basis by 45° . As illustrated in the space-time diagram shown in Fig. 1c, in the single-photon regime, t_{diff} reveals the segment position, whereas t_{sum} is a constant regardless of the position.

To characterize the delay line and the uniformity of the segments, we operated the detector in the single-photon regime and constructed a 1D histogram for the difference time (see Supplementary Fig. 4 for the sum time). As shown in Fig. 1d, the difference time histogram consisted of 16 Gaussians. The full-width at half-maximum (FWHM) was 20.3 ± 0.6 ps (average value with 1σ uncertainty), and the standard deviation of the peak amplitudes was 6% of their mean.

The 429- μ m-long delay line between adjacent detectors created an 86.8 ± 0.3 ps delay, corresponding to a signal propagation speed of $0.016c$. The anomalously slow group velocity was due to the high kinetic inductance of the superconducting nanowire and large capacitance offered by the top ground plane placed 450 nm above the nanowire³⁷. Instead of a full field solution^{38–40}, the characteristic impedance and phase velocity of our nanowire transmission line was estimated using a distributed circuit model, where $Z_0 = \sqrt{L_s/C_s}$ and $v_p = 1/\sqrt{L_s C_s}$. Here, $L_s = L'_K + L'_F \approx L'_K$, where L'_K and L'_F are the kinetic and Faraday inductances per unit length, respectively; and C_s is the specific capacitance. From numerical simulation, we estimated $L_s \approx 0.3$ mH m⁻¹ (0.3 nH μ m⁻¹) and $C_s \approx 128$ pF m⁻¹ (0.128 fF μ m⁻¹).

Analysis in a four-element detector

For clarity, we performed detailed timing and photon counting analysis on a widely separated four-element (D_1 – D_4) detector array. The four-element detector had the same design as the sixteen-element device but with a five times longer delay between adjacent segments.

Figure 2a shows 200 pairs of electrical pulses from the detector when illuminated using a sub-ps pulsed laser in the single-photon regime. The pulses were aligned according to the timing reference from the laser. The dashed line marks the trigger level for time tagging, where the four groups of pulses were separated by ~ 426 ps.

Depending on the position of the firing segment, the output pulse shapes were different. This position dependence was due to signal reflections in the nanowire. Besides the major impedance mismatch between the nanowire (1.5 k Ω) and the readout (50 Ω), the resistive hotspot (a dynamic resistance on the k Ω scale) also contributed to reflections. The reflections caused distinct pulse shapes for each detection case. For instance, the pulses from D_1 on Ch1 had two rising edges separated by ~ 3 ns, which matched the round trip time in the nanowire. Due to symmetry, pulses from D_4 on Ch2 also had the same feature. Impedance matching tapers could in principle be used to minimize reflections, enhance signal levels and provide faster rising edges to reduce timing jitter³¹. In our case, instead of performing a perfect impedance matching with a centimetre-long taper, we used a short taper with high cut-off frequency. Though the imperfect impedance matching resulted in large reflections, it was possible to trigger at a lower threshold to capture only the

initial part of the rising edge. Also, as will be shown later, the distinctive pulse shapes caused by reflection actually enabled us to resolve more than two photons.

We demonstrated the detector's ability to resolve single- and two-photon events by performing a photon-statistics measurement of a coherent source. The measured photon statistics $Q(k)$ are related to the source distribution $S(m)$ by $Q(k) = \sum_{m=0}^{\infty} P(k|m)S(m)$, where $P(k|m)$ is the conditional probability that k detector segments click given m photons in the source. The laser diode serving as the input in our experiment follows the Poisson distribution, $S(m) = \sum_0^{\infty} \frac{\mu^m}{m!} e^{-\mu}$, where μ is the mean photon number. Figure 2b

shows the measured $Q(k)$ when the effective mean photon per pulse of the input laser $\tilde{\mu}$ was attenuated from 2.7 to 0.0027 using a calibrated variable attenuator. The measurement result (symbols) matched our theoretical model (lines, see Methods section for the derivation). Here, $\tilde{\mu} = \eta\mu$ included detector and coupling efficiencies. The value of $\tilde{\mu}$ was estimated by fitting the measured zero-photon probability to $e^{-\tilde{\mu}}$ based on the known attenuation value. For each mean photon number, we accumulated 100,000 detection events (not including non-click events) and extracted the one- and two-photon detection probabilities using the timing logic. The zero-photon probability was measured separately by counting the number of non-click events over 50,000 photon pulses. Doing so ensured enough samples for low-probability events and minimized measurement shot noise, while avoiding the unnecessarily large number of measurements for high probability events.

Figure 2c shows the timing distribution for $\tilde{\mu} = 0.0027$ (left panel) and $\tilde{\mu} = 2.7$ (right panel). When $\tilde{\mu} = 0.0027$, the detector was operating in the single-photon regime, and only the four diagonal groups were present. When $\tilde{\mu} = 2.7$, the six off-diagonal groups became prominent. Here, each 2D histogram was constructed from $\sim 100,000$ detection events. In these measurements, the probing laser had a FWHM pulse width of ~ 200 ps. Therefore, the spread of each detection group in the 2D histogram was significantly wider than that shown in Fig. 1c.

The spread of the timing distribution was affected by both the device timing jitter and the laser pulse width. As shown in Fig. 2c, the single-photon events, compared to the two-photon events, had a slimmer distribution in the t_{diff} axis. The timing uncertainty for each time tag consists of 3 parts: $\sigma_{t_{12}-t_0}^2 = \sigma_{\text{ph}}^2 + \sigma_{\text{det}}^2 + \sigma_e^2$, where σ_{ph} is the photon arrival jitter, that is the photon could hit the detector at any time in the optical pulse duration; σ_{det} is the detector intrinsic jitter, that is the absorbed photon could trigger a voltage pulse with a variable time delay; and σ_e is the electrical jitter, that is the electrical noise would fluctuate the trigger point on pulse rising edge^{41,42}. The photon arrival jitter introduced by the laser pulse width mimics the uncertainty of the timing reference in many real applications, and restricts the minimum delay required to distinguish photon events from adjacent detectors.

We extracted the timing distributions for four representative groups of detection events and compared them in Fig. 2d. The four groups are (i) weakly illuminated single-photon detection on D_2 , (ii) strongly illuminated single-photon detection on D_2 , (iii) two-photon detection where D_2 and D_3 both fire, and (iv) single-photon detection on D_2 probed using a sub-ps pulsed laser instead of a ~ 200 ps modulated laser diode. The last group is labelled as IRF (instrument response function) in the figure, because the laser pulse width had negligible contribution to the measured timing jitters. For all of the single-photon detection events, the differential timing jitter (left panel) only contained the electrical jitter (σ_e) since both the photon arrival jitter (σ_{ph}) and detector intrinsic jitter (σ_{det}) were cancelled (see curves i, ii and IRF). The measured FWHM differential jitter here was 20 ps. For the two-photon detection cases, however, two segments could absorb photons at different times due to the finite optical pulse width, so the differential jitter also contained

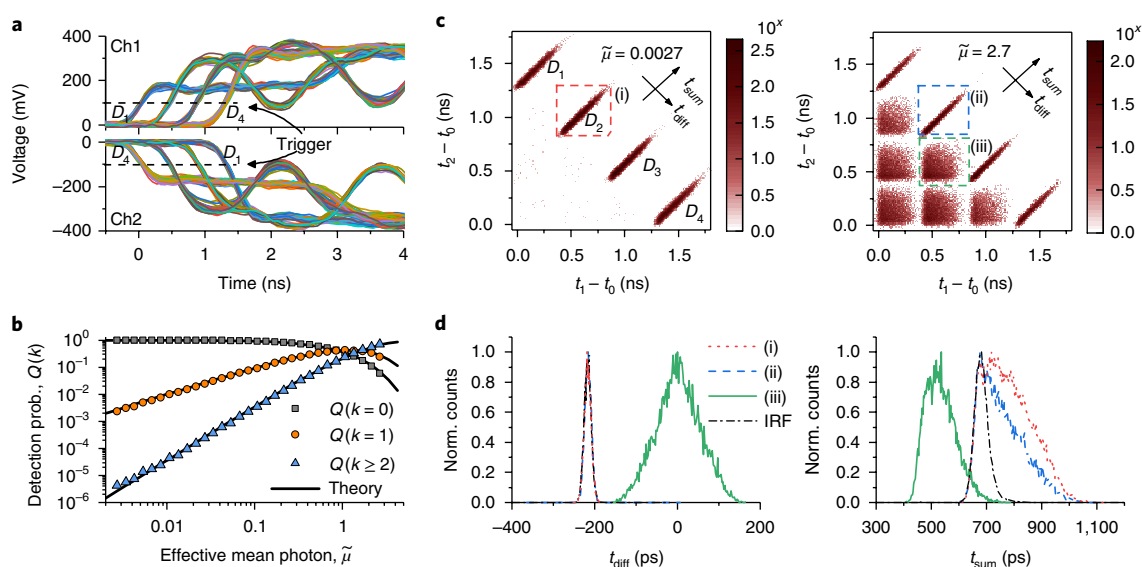


Fig. 2 | Timing-logic-based two-photon detection in a four-element detector chain. **a**, Electrical pulses from a four-element device when illuminated with a sub-ps pulsed laser in the single-photon regime. The dotted lines mark the trigger level for time tagging. **b**, Photon counting statistics under different input powers. $\tilde{\mu} = \eta\mu$ is the effective mean photon per pulse, which included detector efficiency. $Q(k)$ is the probability that k segments fire. The symbols are measurement results and, for comparison, the lines are calculated from a theoretical model based on the detector conditional probability and the Poisson distribution of the coherent state input. **c**, Measured timing distribution for $\tilde{\mu} = 0.0027$ (left) and $\tilde{\mu} = 2.7$ (right) when illuminated using a laser with pulse width of ~ 200 ps. The time bin in the plot is 10 ps and the colour bar is in log scale. **d**, Histogram of the difference (left) and sum (right) time for four representative groups of detection events. (i,ii) D_2 fires under weak (i) and strong (ii) illumination. (iii) D_2 and D_3 fire simultaneously. (i–iii) are labeled in **c** and were measured using a 200 ps pulsed laser. IRF, instrument response function of D_2 probed using a sub-ps pulsed laser in the single-photon regime, showing a FWHM differential jitter of 20 ps and sum jitter of 56 ps.

the photon arrival jitter (σ_{ph} , see curve (iii)). For the sum jitter (right panel), the IRF shows an intrinsic FWHM sum jitter of 56 ps, which was primarily electrical jitter and detector intrinsic jitter. This value is consistent with our previous result in an NbN SNSPD on AlN substrate³⁴. It is noticeable that under strong illumination (ii and iii), the sum jitter became narrower compared to that in the weak illumination case (i). This effect is due to the higher probability of detecting a photon in the early part of a strong optical pulse and is often referred to as ‘pile-up’⁴³.

Two time tags can only resolve up to two-photon events. When three segments fire simultaneously, each readout channel will only register the rising edge from its nearest segment, and the signal from the middle segment will not be time tagged. For instance, when D_2 , D_3 and D_4 fire together, it will produce the same time tags as D_2 and D_4 firing simultaneously. To resolve the difference, we need to process the detailed electrical pulse shapes.

Figure 3a shows traces of 100 pairs of detector pulses from the events where D_2 and D_4 fired (orange traces) or D_2 , D_3 and D_4 fired (blue traces). Despite the large photon-arrival jitter from the 200 ps pulsed laser, these pulses have distinct signatures that allow them to be distinguished (for example, the opening eye marked in Fig. 3a). In principle, due to the reflections in the nanowire, each detection event will have its own fingerprint in the output pulse shape. By learning and discriminating these pulse shapes, one can resolve all the events without ambiguity. In the Supplementary Information, we show a complete list of all 15 observed pulse shapes and their fingerprints (Supplementary Figs. 8–12) and provide more detailed discussions.

In Fig. 3b we demonstrated the capability of resolving up to four photons using the four-element detector. The input optical field was attenuated from an effective mean photon per pulse of 2.7 to 0.27. The maximum effective mean photon number was mainly limited by the sparse and small active area of the detector ($<10^{-5}$ of the illumination area), the unpolished backside of

the chip (scattered $\sim 60\%$ of the light), and illumination power ($\sim 4 \times 10^6$ photons per pulse). For each measured attenuation level, we acquired 50,000 pairs of detector pulses. By analysing the pulse shapes, we discriminated all $2^4 - 1$ combinations of detection cases and sorted them into one-, two-, three- and four-photon events. The zero-photon probability was measured in the same way as in Fig. 2b.

Discussions on optical coupling and scalability

The detector in our experiment was broadband responsive and had saturated internal quantum efficiency at 780 nm wavelength (see Supplementary Fig. 3 for efficiency characterization at different photon energies). Based on previous results³⁴, a 60-nm-wide 2-SNAP using the same material and substrate can saturate at 1,550 nm. The optical absorption can in principle approach unity when the detector is integrated onto a photonic waveguide^{18,44}. More details on waveguide integration and optical absorption can be found in Supplementary Section 4.

The microstrip architecture used here offers significant advantages. When used as a free-space or fibre-coupled detector, the ground plane and dielectric spacer can form an optical cavity to enhance absorption⁴⁵. Compared to co-planar waveguides, the microstrip can be meandered with a higher fill-ratio without having light-absorbing ground plane around the nanowire, which is suitable for high-efficiency single-photon imagers³¹.

The number of segments in the detector can be increased without additional biasing/readout resources. However, the maximum counting rate will decrease due to the kinetic inductance limit⁴⁶. Our current sixteen-element detector had a maximum counting rate of 4.8 MHz (see Supplementary Fig. 5). With increasing segments, the timing logic remains simple, but the pulse shape analysis may become challenging. We are currently building physical and mathematical models to simulate and understand the detailed pulse shapes in the detector.

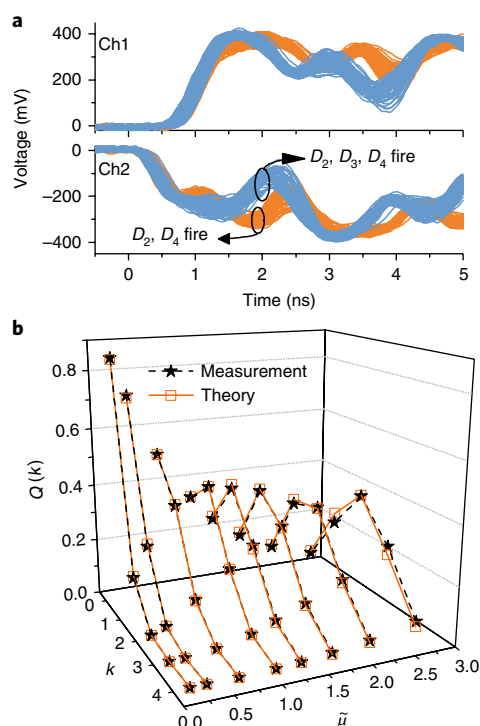


Fig. 3 | Resolving more than two photons based on pulse shape processing. **a**, Traces of 100 pairs of detector pulses, corresponding to detection events where D_2 and D_4 fired, or D_2 , D_3 and D_4 fired. These events are indistinguishable based on timing logic since they have identical timing tags, but can be resolved from their pulse shapes. **b**, Measured photon statistics $Q(k)$ for k up to four under coherent source illumination with mean photon per pulse μ from 0.27 to 2.7. 50,000 pairs of detection pulses were processed for each mean photon number, and the error of each data point was limited by the measurement shot noise.

The current device with relatively small active area was designed for future waveguide integration. To implement an array of large-area detectors for free-space or fibre coupling, the detector segment needs to be designed as an impedance matched meander to allow uninterrupted propagation of electrical signals along the detector. However, due to the large kinetic inductance associated with each segment, the reset time will then become long. Some potential solutions to this issue include using a high-impedance readout to reduce the L/R time constant, or using an a.c./pulsed bias to gate the detector through impedance matched terminals.

Conclusions

We have developed a scalable coincidence detector based on superconducting nanowires. We engineered the nanowire to a microstrip transmission line with a group velocity as low as $0.016c$. By varying the width at different sections, the nanowire serves either as a photon-sensitive detector segment or a compact delay line. The timing-logic operation is ideal for two-photon coincidence counting over large numbers of spatial modes, while the pulse-shape processing can be used for higher-order coincidence measurements in relatively small arrays. The device architecture is suitable for integration on optical waveguides and cavities. With increasing number of detector segments, we expect it to provide a practical solution for large-scale photonic quantum information processing systems.

Methods

Methods, including statements of data availability and any associated accession codes and references, are available at <https://doi.org/10.1038/s41565-018-0160-9>.

Received: 27 November 2017; Accepted: 3 May 2018;
Published online: 4 June 2018

References

- Monroe, C. & Kim, J. Scaling the ion trap quantum processor. *Science* **339**, 1164–1169 (2013).
- Childress, L., Walsworth, R. & Lukin, M. Atom-like crystal defects: from quantum computers to biological sensors. *Phys. Today* **67**, 38–43 (2014).
- Pant, M., Choi, H., Guha, S. & Englund, D. Percolation based architecture for cluster state quantum computation using photon-mediated entanglement between atomic memories. Preprint at <https://arxiv.org/abs/1704.07292> (2017).
- Nemoto, K. et al. Photonic architecture for scalable quantum information processing in diamond. *Phys. Rev. X* **4**, 031022 (2014).
- Peruzzo, A. et al. Quantum walks of correlated photons. *Science* **329**, 1500–1503 (2010).
- Spring, J. B. et al. Boson sampling on a photonic chip. *Science* **339**, 798–801 (2013).
- Broome, M. A. et al. Photonic boson sampling in a tunable circuit. *Science* **339**, 794–798 (2013).
- Tillmann, M. et al. Experimental boson sampling. *Nat. Photon.* **7**, 540–544 (2013).
- Aspuru-Guzik, A. & Walther, P. Photonic quantum simulators. *Nat. Phys.* **8**, 285–291 (2012).
- Kok, P. et al. Linear optical quantum computing with photonic qubits. *Rev. Mod. Phys.* **79**, 135 (2007).
- Hadfield, R. Single-photon detectors for optical quantum information applications. *Nat. Photon.* **3**, 696–705 (2009).
- Natarajan, C. M., Tanner, M. G. & Hadfield, R. H. Superconducting nanowire single-photon detectors: physics and applications. *Supercond. Sci. Technol.* **25**, 063001 (2012).
- Marsili, F. et al. Detecting single infrared photons with 93% system efficiency. *Nat. Photon.* **7**, 210–214 (2013).
- Najafi, F. et al. Fabrication process yielding saturated nanowire single-photon detectors with 24-ps jitter. *IEEE J. Sel. Top. Quantum Electron.* **21**, 3800507 (2015).
- Marsili, F. et al. Efficient single photon detection from 500 nm to 5 μ m wavelength. *Nano Lett.* **12**, 4799–4804 (2012).
- Shibata, H., Shimizu, K., Takesue, H. & Tokura, Y. Ultimate low system dark-count rate for superconducting nanowire single-photon detector. *Opt. Lett.* **40**, 3428–3431 (2015).
- Sprengers, J. P. et al. Waveguide superconducting single-photon detectors for integrated quantum photonic circuits. *Appl. Phys. Lett.* **99**, 181110 (2011).
- Pernice, W. et al. High-speed and high-efficiency travelling wave single-photon detectors embedded in nanophotonic circuits. *Nat. Commun.* **3**, 1325 (2012).
- Reithmaier, G. et al. On-chip generation, routing, and detection of resonance fluorescence. *Nano Lett.* **15**, 5208–5213 (2015).
- Schuck, C., Pernice, W. H. P. & Tang, H. X. NbTiN superconducting nanowire detectors for visible and telecom wavelengths single photon counting on Si_3N_4 photonic circuits. *Appl. Phys. Lett.* **102**, 051101 (2013).
- Najafi, F. et al. On-chip detection of non-classical light by scalable integration of single-photon detectors. *Nat. Commun.* **6**, 5873 (2015).
- Rath, P. et al. Superconducting single photon detectors integrated with diamond nanophotonic circuits. *Light Sci. Appl.* **4**, e338 (2015).
- Vetter, A. et al. Cavity-enhanced and ultrafast superconducting single-photon detectors. *Nano Lett.* **16**, 7085–7092 (2016).
- Shaw, M. et al. Arrays of WSi superconducting nanowire single photon detectors for deep space optical communications. In *Conference on Lasers and Electro-Optics JTh2A.68* (2015).
- Dauler, E. A. et al. Photon-number-resolution with sub-30-ps timing using multi-element superconducting nanowire single photon detectors. *J. Mod. Opt.* **56**, 364–373 (2009).
- Miki, S. et al. Superconducting single photon detectors integrated with single flux quantum readout circuits in a cryocooler. *Appl. Phys. Lett.* **99**, 111108 (2011).
- Allman, M. S. et al. A near-infrared 64-pixel superconducting nanowire single photon detector array with integrated multiplexed readout. *Appl. Phys. Lett.* **106**, 192601 (2015).
- Doerner, S., Kuzmin, A., Wuensch, S., Charaev, I. & Siegel, M. Operation of multipixel radio-frequency superconducting nanowire single-photon detector arrays. *IEEE Trans. Appl. Supercond.* **27**, 2201005 (2017).
- Doerner, S. et al. Frequency-multiplexed bias and readout of a 16-pixel superconducting nanowire single-photon detector array. *Appl. Phys. Lett.* **111**, 032603 (2017).
- Hofherr, M. et al. Time-tagged multiplexing of serially biased superconducting nanowire single-photon detectors. *IEEE Trans. Appl. Supercond.* **23**, 2501205 (2013).
- Zhao, Q.-Y. et al. Single-photon imager based on a superconducting nanowire delay line. *Nat. Photon.* **11**, 247–251 (2017).

32. Divochiy, A. et al. Superconducting nanowire photon-number-resolving detector at telecommunication wavelengths. *Nat. Photon.* **2**, 302–306 (2008).
33. Zhao, Q. et al. Superconducting-nanowire single-photon-detector linear array. *Appl. Phys. Lett.* **103**, 142602 (2013).
34. Zhu, D. et al. Superconducting nanowire single-photon detector on aluminum nitride. In *Conference on Lasers and Electro-Optics FTu4C.1* (2016).
35. Ejrnaes, M., Cristiano, R., Quaranta, O., Pagano, S. & Gaggero, A. A cascade switching superconducting single photon detector. *Appl. Phys. Lett.* **91**, 262509 (2007).
36. Calandri, N., Zhao, Q.-Y., Zhu, D., Dane, A. & Berggren, K. K. Superconducting nanowire detector jitter limited by detector geometry. *Appl. Phys. Lett.* **109**, 152601 (2016).
37. Pippard, A. B. The surface impedance of superconductors and normal metals at high frequencies III. The relation between impedance and superconducting penetration depth. *Proc. R. Soc. Lond. A* **191**, 399 (1947).
38. Mason, P. V. & Gould, R. W. Slow-wave structures utilizing superconducting thin-film transmission lines. *J. Appl. Phys.* **40**, 2039–2051 (1969).
39. Swihart, J. C. Field solution for a thin-film superconducting strip transmission line. *J. Appl. Phys.* **32**, 461–469 (1961).
40. Chang, W. H. The inductance of a superconducting strip transmission line. *J. Appl. Phys.* **50**, 8129–8134 (1979).
41. Sidorova, M. et al. Physical mechanisms of timing jitter in photon detection by current-carrying superconducting nanowires. *Phys. Rev. B* **96**, 184504 (2017).
42. Zhao, Q. et al. Intrinsic timing jitter of superconducting nanowire single-photon detectors. *Appl. Phys. B* **104**, 673–678 (2011).
43. Becker, W. *Advanced Time-Correlated Single Photon Counting Techniques* (Springer-Verlag, Heidelberg, 2005).
44. Hu, X., Holzwarth, C. W., Masciarelli, D., Dauler, E. A. & Berggren, K. K. Efficiently coupling light to superconducting nanowire single-photon detectors. *IEEE Trans. Appl. Supercond.* **19**, 336–340 (2009).
45. Rosfjord, K. M. et al. Nanowire single-photon detector with an integrated optical cavity and anti-reflection coating. *Opt. Express* **14**, 527 (2006).
46. Kerman, A. J. et al. Kinetic-inductance-limited reset time of superconducting nanowire photon counters. *Appl. Phys. Lett.* **88**, 111116 (2006).

Acknowledgements

We thank J. Daley and M. Mondol for technical support in nanofabrication; C. Chen and F. F. C. Wong for use of their electro-optic modulator; E. Toomey, B. Butters, C.-S. Kim and the QNN-SNSPD team for discussion and assistance. This research was supported by the Air Force Office of Scientific Research grant under contract number FA9550-14-1-0052; National Science Foundation grant under contract number ECCS-1509486; and the DARPA Detect programme through the Army Research Office under cooperative agreement number W911NF-16-2-0192. D.Z. was supported by a National Science Scholarship from A*STAR, Singapore. H.C. was supported in part by a Samsung Scholarship. T.-J.L. was supported by the Department of Defense National Defense Science and Engineering Graduate Fellowship. A.E.D. was supported by a National Aeronautics and Space Administration Space Technology Research Fellowship (award number NNX14AL48H).

Author contributions

D.Z., Q.-Y.Z., K.K.B. and D.E. conceived and designed the experiment. D.Z. designed the device. D.Z. and T.-J.L. fabricated the device. D.Z., Q.-Y.Z. and H.C. performed the measurement. D.Z. and A.E.D. deposited the superconducting film. K.K.B. and D.E. supervised the project. All authors discussed the results and contributed to writing the paper.

Competing interests

A related patent (WO2017136585A1) was filed by Q.-Y.Z. and K.K.B. through MIT.

Additional information

Supplementary information is available for this paper at <https://doi.org/10.1038/s41565-018-0160-9>.

Reprints and permissions information is available at www.nature.com/reprints.

Correspondence and requests for materials should be addressed to Q.-Y.Z. or K.K.B.

Publisher's note: Springer Nature remains neutral with regard to jurisdictional claims in published maps and institutional affiliations.

Methods

Detector fabrication. The NbN film was deposited on an AlN-on-sapphire substrate (Kyma Technologies) using d.c. magnetron sputtering at 840 °C. The NbN deposition and nanowire patterning follows that described previously¹⁴. The AlN was c-axis oriented with a thickness of 200 ± 5 nm. The NbN film had a thickness of ~5 nm, critical temperature of 10.7 K, transition width of 1.63 K, sheet resistance of $510 \Omega \text{sq}^{-1}$, and residual resistance ratio of 0.85. The gold contact pads were patterned using photolithography followed by metal evaporation (5 nm Ti/50 nm Au/5 nm Ti) and lift-off. The superconducting nanowires were patterned using electron-beam lithography (Elionix F125) with a negative-tone resist, hydrogen silsesquioxane (HSQ), and etched using CF_4 reactive-ion etching. The dielectric spacer was fabricated by spin-coating the sample with a flowable oxide (Dow Corning FOX-16) and curing the intended area with electron beam exposure. The thickness of the oxide spacer was measured to be 450 nm using a surface profiler (Dektak). The top grounding plane was fabricated with an aligned photolithography followed by metal evaporation and lift-off (5 nm Ti and 60 nm Au). See Supplementary Fig. 1 for the detailed process flow.

Detector measurement. All measurements were performed in a pulse-tube-based cryostat at 3.0 K. Each detector was wire bonded to a printed circuit board and connected to room-temperature readout circuits through a pair of SMP cables (Ch1 and Ch2). The d.c. bias current was injected from Ch1 using a bias tee. The RF signal from each channel was amplified using a low-noise amplifier (MITEQ AM-1309, gain: 50 dB, bandwidth: 1 kHz–1 GHz) and acquired using a 6 GHz real-time oscilloscope (Lecroy 760Zi) or counted using a 225 MHz universal counter (Agilent 53132A). The detector chip was back illuminated through a single-mode optical fibre (SMF-28e). The fibre was mounted on a piezo-stage (Attocube) for alignment and focusing. When measuring the sixteen-element detector and probing the intrinsic timing response of the four-element detector, a sub-picosecond fibre-coupled mode-locked laser (Calmar FPL-02CCF) was used. It has a centre wavelength of 1,550 nm and repetition rate of 20 MHz. During the experiment, the repetition rate was reduced to 500 kHz using an electro-optic modulator. When measuring the multi-photon response of the four-element detector, a 1,550 nm modulated diode laser was used (PicoQuant LDH-P-C-1550 laser head with PDL 800-B driver). The optical pulse was asymmetric, non-Gaussian, with a width of >200 ps (see Supplementary Fig. 7 for the pulse shape estimation). The repetition rate was set to 1 MHz. In both cases, the laser output was split into two paths, one to a fast photodetector (Thorlabs DET08CFC) as the

timing reference, and the other to the detector with a calibrated variable attenuator (JDSU HA9) and a polarization controller. More details on the characterization of standard detector metrics can be found in Supplementary Section 2.

Derivation for photon counting statistics. In the generic case, when an optical mode illuminates on an N -element detector, each photon has probability c_i of reaching detector D_i with a detection efficiency η_i . c_i depends on the spatial mode of the input field, while η_i is intrinsic to the detector. To simplify the modelling, we assumed a uniform detection efficiency for all elements (that is, $\eta_i = \eta_j = \eta$). This assumption is reasonable based on our experimental characterization. We measured the detection efficiency distribution by driving the probing fibre far away from the device and uniformly illuminating the detector. For both the four-element and sixteen-element detector chains, the standard deviation in η_i was <6% of its mean (see Fig. 1e and Supplementary Fig. 6). Under this assumption, we treated each segment as a perfect detector with unity efficiency and incorporated the actual detector efficiency to the input field, which makes the input mean photon number $\tilde{\mu} = \eta\mu$. Here, we also included coupling efficiencies to μ so that $\sum c_i = 1$.

For $\eta_i = 1$ and $\sum c_i = 1$, the conditional probability for m input photon and k detector output, $P(k|m)$, can be evaluated as

$$P(k|m) = \sum_{l_1, l_2, \dots, l_N=0}^m C_{l_1}^m c_1^{l_1} \times C_{l_2}^{m-l_1} c_2^{l_2} \times \dots \times C_{l_N}^{l_N} c_N^{l_N} \quad (1)$$

$$= \sum_{l_1, l_2, \dots, l_N=0}^m m! \times \frac{c_1^{l_1}}{l_1!} \times \frac{c_2^{l_2}}{l_2!} \times \dots \times \frac{c_N^{l_N}}{l_N!}$$

where l_i denotes the number of photons arriving on detector D_i ; $\{l_1, l_2, \dots, l_N\}$ has k non-zero terms and $\sum l_i = m$; $C_y^x = \frac{x!}{y!(x-y)!}$ is the combination operation. This expression can be evaluated numerically with $O(m^N)$ complexity, which is tractable for a four-element detector. In the experiment, c_i values were characterized by measuring the counting distribution in the single-photon regime (see Supplementary Fig. 6 for the measurement of c_i).

Data availability. The data that support the plots within this paper and other findings of this study are available from the corresponding authors upon reasonable request.